Optics Letters

Topological edge states of a long-range surface plasmon polariton at the telecommunication wavelength

Ran Gladstein Gladstone,[1,*] Sukrith Dev,[2] Jeffery Allen,[2] Monica Allen,[2] and Gennady Shvets[1]

[1]School of Applied and Engineering Physics, Cornell University, Ithaca, New York, 14853, USA
[2]Air Force Research Laboratory, Munitions Directorate, 101 W. Eglin Blvd, Eglin AFB, Florida 32542, USA
*Corresponding author: rag298@cornell.edu

Received 25 July 2022; revised 16 August 2022; accepted 16 August 2022; posted 17 August 2022; published 29 August 2022

Confining light by plasmonic waveguides is promising for miniaturizing optical components, while topological photonics has been explored for robust light localization. Here we propose combining the two approaches into a simple periodically perforated plasmonic waveguide (PPW) design exhibiting robust localization of long-range surface plasmon polaritons. We predict the existence of a topological edge state originating from a quantized topological invariant, and numerically demonstrate the viability of its excitation at telecommunication wavelength using near-field and waveguide-based approaches. Strong modification of the radiative lifetime of dipole emitters by the edge state, and its robustness to disorder, are demonstrated.

https://doi.org/10.1364/OL.471442

Compactness and robustness are among the most desirable features of any photonic system. Compactness enables fitting multiple photonic components, such as waveguides, delay lines, or modulators, on a single chip. One of the fundamental approaches to achieving compactness is to replace standard dielectric components with metallic ones: hence the emergence of plasmonics [1–4] as one the most exciting sub-fields of optics. However, robustness enables reflectionless propagation or spatial localization even in the presence of finite disorder. Topological photonics, which takes advantage of the conservation of quantized topological invariants [5,6], has been proposed as a promising approach to ensure robustness to certain types of defects and disorder [7].

Implementing topologically nontrivial photonic structures using plasmonic platforms (including the ones based on two-dimensional materials [8,9]) is a natural step to achieving both features. However, several challenges must be overcome to achieve this objective. Because many underlying concepts of topological photonics rely on Hermitian physics, this can be a serious limitation for inherently lossy plasmonic platforms. Nevertheless, open (i.e., non-Hermitian) photonic systems with loss and/or gain have been shown to exhibit topological robustness [10–14]. Intrinsic material losses are particularly severe for plasmonic platforms. Difficult to compensate, such Ohmic losses are particularly high in the vicinity of resonances that provide the necessary negative permittivity for plasmonics. One method that has been successfully used is to create a hybrid platform of dielectrics and plasmonic nanostructures [15]. Another method to mitigate the Ohmic losses in plasmonic devices is by modifying their material composition or geometry [16]. For example, a finite metal strip can support multiple plasmonic modes of different symmetries and spatial dimensions [17]. The long-range surface plasmon polariton (LRSPP) has particularly low losses as it propagates along the strip [2] because it is localized mostly in the dielectric region, i.e., outside of the lossy plasmonic material.

In this Letter, we use the LRSPP to overcome material losses in plasmonic systems and demonstrate a realizable plasmonic topological structure emulating the simplest one-dimensional (1D) topological insulator inspired by the Su–Schrieffer–Heeger (SSH) model [18]. Such a system can be part of an integrated photonic circuit for communications and sensing applications. We begin with the unit cell design and discuss the origin of low losses and the bulk topological invariant that gives rise to a topological edge state. Next, we present two methods of exciting the topological edge state using: (i) a judiciously placed point dipole simulating a near-field scanning optical microscopy (NSOM) experiment [19]; and (ii) LRSPP waveguides as input and output channels [20].

The periodic topological structure analyzed in this Letter is shown in Fig. 1(a). It comprises a gold strip waveguide periodically perforated along the propagation direction x of the LRSPPs, and is sandwiched between a quartz ($n_{\text{sub}} = 1.5$ refractive index) and air region. Each waveguide period contains two half-circular holes on each side of the strip as shown in Fig. 1(a), bottom. We note that other hole shapes and locations would work just as well as long as inversion symmetry is maintained. LRSPP modes of the unperforated plasmonic strip are characterized by their continuous wavenumber k along the waveguide and their complex-valued frequency $\omega_0 \equiv 2\pi f_0(k) + i\nu_0$, where f_0 is the vacuum frequency and ν_0 is the decay rate. For convenience, the continuous spectrum $f_0(k)$ of LRSPPs is presented in Fig. 1(b)

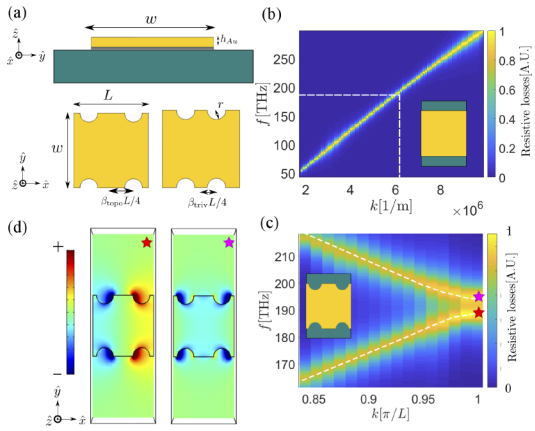

Fig. 1. Bulk design of LRSPP topological insulator. (a) Structure geometry. Top and side views of topological (left) and trivial (right) unit cell designs. Yellow, Au; gray, Cr; teal, quartz. Parameters: $L = w = 500\,\text{nm}$; $r = 70\,\text{nm}$; $\beta_{\text{topo}} = 1.2$; $\beta_{\text{triv}} = 0.8$; $h_{\text{Au}} = 45\,\text{nm}$; $h_{\text{Cr}} = 5\,\text{nm}$; and the substrate is semi-infinite. (b), (c) Band structures $f(k)$ of LRSPPs in (b) un-patterned and (c) periodically perforated plasmonic waveguides presented as normalized Lorentzian line shape at resonance peaks. Dashed white lines in panel (b), targeted LRSPP with $\lambda_0 = \lambda_{\text{TC}} = c/f_{\text{TC}}$. Inset, unit cell. White dashed lines in panel (c), band centers. Pink (red) star, the wavelengths $\lambda_{\pm}$ of the symmetric (anti-symmetric) Bloch LRSPPs shown in panel (d). (d) Electric field E_x of the modes marked as stars in panel (c).

in the form of Lorentzian line shape $A_0(k,f)$ according to the value of ν_0 (see Supplement 1).

For the periodically perforated plasmonic waveguide (PPW), Bragg scattering of LRSPPs by the holes introduces two propagation bands separated by a bandgap. Two such bands $f_{\pm}(k)$ and the bandgap are visualized in Fig. 1(c) as $A_{\text{res}}(k,f)$ obtained using three-dimensional COMSOL Multiphysics simulations, where the Bloch LRSPPs characterized by the Bloch wavenumber k are driven using randomly placed/oriented electric dipoles [21] oscillating with frequency $\omega \equiv 2\pi c/\lambda$. To ensure a propagation bandgap around a telecommunication (TC) wavelength $\lambda_{\text{TC}} \approx 1.55\,\mu\text{m}$, we have chosen the $x-$periodicity (unit cell length L) as $L = 500\,\text{nm}$. The details of calculating $A_{\text{res}}(k,f)$ for the un-patterned and periodically perforated plasmonic waveguides, as well as the optical properties of gold and the adhesive chromium nano-layer are discussed in Supplement 1. Geometric dimensions of the plasmonic strip waveguide are given in the caption of Fig. 1.

Assuming that the center of a given hole is unequally spaced between its left and right immediate neighbors, two types of mirror-symmetric with respect to $y-z$ midplane unit cells can be chosen as shown in Fig. 1(a): topological and trivial. The center-to-center distance between the 1st (left) and 2nd (right) holes, expressed as $\beta L/2$, determines topological properties of the unit cell: $\beta \equiv \beta_{\text{topo}} > 1$ for the topological, and $\beta \equiv \beta_{\text{triv}} < 1$ for the complementary trivial unit cells, as shown in Fig. 1(a), bottom. The main difference between topological and trivial unit cells is the symmetry of the propagation bands below and above the bandgap. The topological unit cell has a band below (above) the bandgap that is anti-symmetric (symmetric) with respect to the $y-z$ midplane, as shown in Fig. 1(d). The opposite is true for the trivial unit cell (see Supplement 1). This type of band inversion is related to a topological invariant known as the Zak phase ϕ_Z [22] (see Supplement 1 for definition).

While generalizations of the Zak phase for non-Hermitian systems with chiral symmetry have been introduced [23], our system lacks chiral symmetry due to long-range interactions of the plasmonic modes. Nevertheless, our system maintains inversion symmetry in the $\hat{x}$ direction which quantizes the Zak phase to just two possible values: $\phi_Z = 0, \pi$ [24,25]. For the topological (trivial) unit cell, we find the Zak phase equal to $\phi_Z^{\text{topo}} = \pi$ ($\phi_Z^{\text{triv}} = 0$). This can be calculated according to the symmetry of the modes in Fig. 1(d) and by noting that as $k \to 0$ (the long wavelength limit), the LRSPP mode is symmetric [2,22] (see Supplement 1). An implication of the quantized Zak phase of ϕ_Z^{topo} is a filling anomaly [26] that introduces an additional (edge) state at the interface with a trivial domain. However, for the edge state to be spectrally pinned to the midgap frequency, an additional (chiral) symmetry is required [25].

While the PPW shown in Fig. 1 clearly does not posses global chiral symmetry across the entire Brillouin zone (BZ), it does locally around the edge of the BZ, as can be observed in Fig. 1(c) from the symmetric band structure around $X = \pi/L$. To show this local chiral symmetry, we use an expansion model in the vicinity of the BZ edge using the following two-band Hamiltonian $H(q)$, which is the function of $q = X - k$:

$$H(q) = \Delta_x \hat{\sigma}_x + q\Delta_z \hat{\sigma}_z + i\Delta_0^{\text{NH}} \hat{\sigma}_0 + i\Delta_x^{\text{NH}} \hat{\sigma}_x, \tag{1}$$

where $H(q)$ is expressed on the basis of the symmetric and anti-symmetric eigenstates of the inversion operator shown in Fig. 1(d). Here, $\Delta_x, \Delta_z, \Delta_0^{\text{NH}}, \Delta_x^{\text{NH}}$ are real-valued coefficients, $\hat{\sigma}_0$ is the 2×2 identity matrix, and $\hat{\sigma}_x, \hat{\sigma}_z$ are the first and third Pauli matrices, respectively. If losses are neglected, the system respects bosonic time-reversal symmetry, which is expressed as complex conjugation. Hence, the Hamiltonian $H(q)$ does not contain Hermitian terms proportional to $\hat{\sigma}_y$. The first two terms describe the finite-mass (from $\Delta_x \neq 0$) Hermitian 1D Dirac Hamiltonian. The non-Hermitian terms in $H(q)$ describe the lowest-order shared (third term) and differential (fourth term) loss rates, respectively.

It can be shown (see Supplement 1) that the anti-symmetric and symmetric modes have very similar Ohmic loss rates because of their similar penetration into the plasmonic material. Therefore, only the third term in Eq. (1) needs to be retained, and the chiral symmetry is broken in a trivial manner [24], making the bulk topological classification of the non-Hermitian model equivalent to the Hermitian classification. To establish the existence of a midgap-pinned edge state, we note that the value of the Berry connection $A(k)$—the quantity proportional to the k-derivative of the Berry phase used to calculate the Zak phase according to $\phi_Z = \int_{-X}^{X} dk A(k)$—is inversely proportional to the bandgap size at k [18]. Therefore, as long as the bandgap size is small compared to the entire energy spectrum, the only contributions to the Zak phase are localized near the minima of the bandgap in k, i.e., at $k = X$ (see Supplement 1). Because the contributions to the Zak phase originate only near the BZ edges, where a local chiral symmetry approximately exists to the lowest order in q, an edge mode (if present) must be pinned to the midgap frequency [25].

This conclusion is confirmed in Fig. 2(a), where topological and trivial semi-infinite PPWs are interfaced to form a domain wall (red and blue dashed lines), and an edge

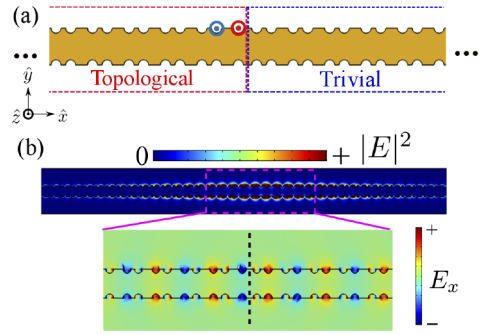

Fig. 2. Topologically robust edge state of long-range SPPs in a periodically perforated plasmonic waveguide. (a) A domain wall between semi-infinite topological (left) and trivial (right) PPWs supports a localized edge state that strongly (weakly) couples to an electric dipole emitter marked by a blue (red) circle. The emitter is placed inside the first (second) holes of the topological waveguide. (b) Top: $|E|^2$ of the edge eigenmode concentrated inside the first hole of the topological and trivial waveguides on the two sides of the domain wall. Bottom: E_x field component of the zoomed pink box. Interface marked in dashed black line.

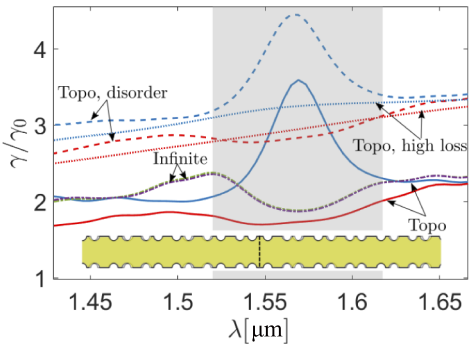

Fig. 3. Purcell factors for two dipole emitters placed inside two adjacent holes of a PPW. Emitter locations (1st and 2nd holes) and color-coding (blue and red), same as in Fig. 2(a). Solid lines, the emitters are placed at the domain wall separating semi-infinite topological and trivial PPWs shown in Fig. 2(a). Dash–dotted lines, infinite PPW. Dashed lines, finite disorder of inter-hole distance in the topological and trivial PPWs. Dotted curves, ×10 increased loss. Shaded gray area, the bandgap wavelengths. Inset shows PPW with no disorder (gray) overlaid with PPW with disorder (yellow). Interface region marked with black dashed line.

mode exponentially localized at the domain wall with an exponential decay length $l_{\text{edge}} \sim 8L \approx 4\,\mu\text{m}$ was revealed using eigenvalue COMSOL simulations. The obtained complex-valued frequency of the edge state is $f_{\text{edge}} \approx (190 + i5)$ THz; its real-valued frequency—corresponding to vacuum wavelength $\lambda_{\text{edge}} \approx 1.58\,\mu\text{m}$—is indeed close to the midgap frequency $\hat{f} \approx 191$ THz, while its decay rate is close to the shared loss rate of the two bulk modes at the edge of the BZ. Moreover, it can be observed from Fig. 2(b) that the distribution of the electric field energy of the edge state is highly unequal between the two perforating holes: it is primarily concentrated in the 1st hole of the PPWs. This is similar to the property of the edge mode described within the SSH model [18]: to occupy only one-half of the lattice sites, with every other site unoccupied. Therefore, it can be expected that: (i) near-field excitation of the edge state by an electrically small antenna (e.g., SNOM tip) or a dipole emitter is strongly dependent on their location inside the unit cell; and (ii) the radiative decay time of an emitter placed in one of the perforating holes close to the domain wall is also modified in a hole-dependent manner.

To verify these predictions, we performed a driven simulation with a dipole emitter oriented in the $\hat{z}$ direction placed at the center of holes 1 and 2 [blue and red circles in Fig. 2(a), respectively] at the domain wall formed by $N = 40$ trivial and topological unit cells on each side. The interaction strength of these two emitters with the photonic structure is expressed by the Purcell factor $F_P(\lambda) = \gamma/\gamma_0 = P(\lambda)/P_0(\lambda)$ equal to the ratio of the powers $P(\lambda)$ and $P_0(\lambda)$ emitted by a dipole with and without the structure, respectively [27] (see Supplement 1). The radiative decay rate $\gamma(\lambda)$ of the emitter is increased in the same proportion. The corresponding Purcell factors color-coded for the two emitter locations (blue and red) are plotted in Fig. 3 for the following cases: (i) a PPW uninterrupted by the domain wall (dot–dashed line); and (ii) a topological device with a domain wall shown in Fig. 2(a) (solid curves).

As expected, case (i) does not reveal any dependence on the emitter location. Moreover, $F_P(\lambda)$ has a dip inside the photonic bandgap $\lambda_- < \lambda < \lambda_+$ (shaded region in Fig. 3), where $\lambda_+ \approx 1.62\,\mu\text{m}$ and $\lambda_- \approx 1.53\,\mu\text{m}$ are the edges of the lower and upper LRSPP propagation bands, respectively. This feature of the Purcell factor is related to the reduction of the density of optical states (DOS) inside the bandgap and, therefore, reduced emitter coupling to the propagating LRSPPs.

An entirely different spectral dependence of the Purcell factor is observed in case (ii). First, for the emitter placed inside hole 1, we observed considerable Purcell factor enhancement (up to $F^{(1)}_{P,\text{topo}} \sim 3.5$) inside the bandgap with respect to its baseline value of $F_P \sim 2$ outside the bandgap. Such dramatic Purcell factor enhancement is not possible in most nanoparticle plasmonic systems [24,28] where the shared loss is significantly larger than the bandgap size, as can be seen from the dotted curves in Fig. 3 generated by increasing the Drude loss by a factor of 10. However, the LRSPPs supported by PPWs have moderate decay rates (of the order of ~ 5 THz at $q = 0$) that are comparable with the bandgap ($\Delta f \sim 10$ THz), thereby enabling preferential coupling of a dipole oscillating at the f_{edge} frequency to the edge state. However, the Purcell factor of the emitter placed inside hole 2 is reduced to $F^{(2)}_{P,\text{topo}} \sim 1.7$. In Ref. [29], qualitatively similar results were obtained but the emitter dipole had to be embedded inside a gold nanoparticle, which is not feasible.

To illustrate the robustness of the edge states to disorder, we introduce randomness in the hole center locations $[x_1, x_2]$ along the entire topological device shown in the inset of Fig. 3. This is done using a uniform random variable $U[-25\,\text{nm}, +25\,\text{nm}]$ (see Supplement 1. Of most importance is that the edge mode frequency does not shift, as predicted by the topological nature of the system. The Purcell factor baseline in Fig. 3 increases due to effective localization in the entire spectrum by multiple scatterings, and the edge mode Purcell enhancement is maintained in relation to the baseline, showing the strength of topological robustness and enabling more robust experimental detection of the edge states using NSOM (see Supplement 1). This approach may also be used in the design of robust plasmonic antennas whose performance is enhanced by the presence of disorder [30].

Next, we examine the excitation of the LRSPP topological edge mode in the context of an integrated photonic circuit.

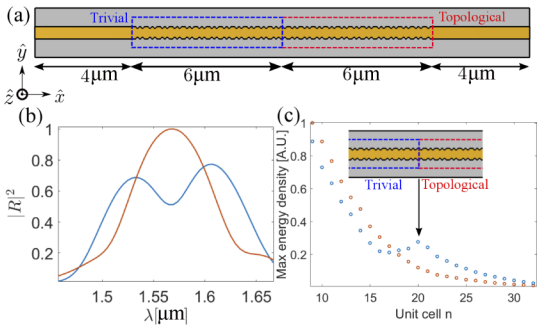

Fig. 4. Waveguide excitation of topological edge mode. (a) LRSPP waveguide with trivial and topological bandgap sections interfacing (topological device). (b) Reflection spectra of trivial device (orange) and topological device (blue) normalized to the maximal value to account for Ohmic losses. (c) Normalized maximum value of the averaged energy density per unit cell for the topological (blue) and trivial (orange) devices at the frequency of the edge mode. Inset shows interface region for the topological device located between unit cells 20 and 21.

The excitation schematic is shown in Fig. 4(a): an unpatterned gapless plasmonic waveguide [see Fig. 1(a)] delivers LRSPPs to a PPW-based topological plasmonic device (12-units-long topological/trivial PPWs on the two sides of the domain wall) discussed above. The reflection plot (blue line) in Fig. 4(b) shows a broad spectral peak covering the entire bandgap, with a narrower dip at midgap. To understand the origin of the broad reflection peak, we substitute the topological portion of the PPW by a trivial one (or vice versa). As expected [20], the bandgap of the resulting trivial (i.e., devoid of the domain wall) device increases reflection (orange curve) and reduces transmission (see Supplement 1). The reflection dip for the topological device is then explained by the tunneling to/from the edge state supported by the domain wall. This is supported by plotting the energy density inside the trivial (orange circles) and topological (blue circles) devices shown in Fig. 4(c). While the former exhibits a purely exponential decay along the length of the device, the latter exhibits a non-monotonic dependence on the distance into the topological device. The energy density peak in the middle of the topological device indicates the excitation of the edge state. We note that the physical dimensions and bandwidth of the topological LRSPP device shown here are encouraging for its application in standard integrated photonic circuits at telecom wavelengths [31].

In summary, we have introduced a realizable plasmonic device operating in the TC band that supports a topological edge mode. The device is based on periodically perforated plasmonic waveguide supporting band-folded LRSPPs. Prohibitively high plasmonic losses that would normally obscure any topological features are circumvented by using lower-loss LRSPP modes. Two different experimentally accessible excitation methods—near-field based and integrated photonics—are proposed, and their corresponding manifestations of the edge state are discussed. Integration of plasmonics and topological photonics opens new opportunities to make nanophotonic devices simultaneously compact and robust.

Funding. Air Force Research Laboratory (20RWCOR090, 22RWCOR002); National Science Foundation (DMR-1719875); Army Research Office (W911NF2110180); Office of Naval Research (N00014-21-1-2056).

Disclosures. The authors declare no conflicts of interest.

Data availability. Data underlying the results presented in this paper are available in Ref. [32].

Supplemental document. See Supplement 1 for supporting content.

REFERENCES

1. S. A. Maier and H. A. Atwater, J. Appl. Phys. **98**, 011101 (2005).
2. P. Berini, Adv. Opt. Photonics **1**, 484 (2009).
3. A. Boltasseva, T. Nikolajsen, K. Leosson, K. Kjaer, M. S. Larsen, and S. I. Bozhevolnyi, J. Lightwave Technol. **23**, 413 (2005).
4. M. Ayata, Y. Fedoryshyn, W. Heni, B. Baeuerle, A. Josten, M. Zahner, U. Koch, Y. Salamin, C. Hoessbacher, C. Haffner, D. L. Elder, L. R. Dalton, and J. Leuthold, Science **358**, 630 (2017).
5. A. B. Khanikaev and G. Shvets, Nat. Photonics **11**, 763 (2017).
6. T. Ma and G. Shvets, New J. Phys. **18**, 025012 (2016).
7. T. Ma and G. Shvets, Phys. Rev. B **95**, 165102 (2017).
8. M. Jung, Z. Fan, and G. Shvets, Phys. Rev. Lett. **121**, 086807 (2018).
9. L. Xiong, C. Forsythe, M. Jung, A. S. McLeod, S. S. Sunku, Y. M. Shao, G. X. Ni, A. J. Sternbach, S. Liu, J. H. Edgar, E. J. Mele, M. M. Fogler, G. Shvets, C. R. Dean, and D. N. Basov, Nat. Commun. **10**, 4780 (2019).
10. S. Malzard, C. Poli, and H. Schomerus, Phys. Rev. Lett. **115**, 200402 (2015).
11. M. A. Bandres, S. Wittek, G. Harari, M. Parto, J. Ren, M. Segev, D. N. Christodoulides, and M. Khajavikhan, Science **359**, eaar4005 (2018).
12. M. Parto, Y. G. N. Liu, B. Bahari, M. Khajavikhan, and D. N. Christodoulides, Nanophotonics **10**, 403 (2020).
13. H. Zhao, X. Qiao, T. Wu, B. Midya, S. Longhi, and L. Feng, Science **365**, 1163 (2019).
14. Z. Zhang, X. Qiao, B. Midya, K. Liu, J. Sun, T. Wu, W. Liu, R. Agarwal, J. M. Jornet, S. Longhi, N. M. Litchinitser, and L. Feng, Science **368**, 760 (2020).
15. H. Zhang, Y. Zheng, Z.-M. Yu, X. Hu, and C. Lu, J. Opt. **23**, 124002 (2021).
16. J.-S. Huang, V. Callegari, P. Geisler, C. Brüning, J. Kern, J. C. Prangsma, X. Wu, T. Feichtner, J. Ziegler, P. Weinmann, M. Kamp, A. Forchel, P. Biagioni, U. Sennhauser, and B. Hecht, Nat. Commun. **1**, 150 (2010).
17. P. Berini, Phys. Rev. B **61**, 10484 (2000).
18. J. K. Asbóth, L. Oroszlány, and A. Pályi, *A Short Course on Topological Insulators: Band Structure and Edge States in One and Two Dimensions*, Vol. 919 of Lecture Notes in Physics (Springer International, 2016).
19. B. Hecht, B. Sick, U. P. Wild, V. Deckert, R. Zenobi, O. J. Martin, and D. W. Pohl, J. Chem. Phys. **112**, 7761 (2000).
20. A. Boltasseva, S. I. Bozhevolnyi, T. Søndergaard, T. Nikolajsen, and K. Leosson, Opt. Express **13**, 4237 (2005).
21. M. Baker, W. Liu, and E. McLeod, Opt. Express **29**, 22761 (2021).
22. M. Xiao, Z. Zhang, and C. T. Chan, Phys. Rev. X **4**, 021017 (2014).
23. S. Lieu, Phys. Rev. B **97**, 045106 (2018).
24. S. R. Pocock, X. Xiao, P. A. Huidobro, and V. Giannini, ACS Photonics **5**, 2271 (2018).
25. Z.-Q. Jiao, S. Longhi, X.-W. Wang, J. Gao, W.-H. Zhou, Y. Wang, Y.-X. Fu, L. Wang, R.-J. Ren, L.-F. Qiao, and X-M. Jin, Phys. Rev. Lett. **127**, 147401 (2021).
26. W. A. Benalcazar, T. Li, and T. L. Hughes, Phys. Rev. B **99**, 245151 (2019).
27. L. Novotny and B. Hecht, *Principles of Nano-Optics* (Cambridge University Press, 2012).
28. I. S. Sinev, I. S. Mukhin, A. P. Slobozhanyuk, A. N. Poddubny, A. E. Miroshnichenko, A. K. Samusev, and Y. S. Kivshar, Nanoscale **7**, 11904 (2015).
29. C. Ling, M. Xiao, C. T. Chan, S. F. Yu, and K. H. Fung, Opt. Express **23**, 2021 (2015).
30. L. Sapienza, H. Thyrrestrup, S. Stobbe, P. D. Garcia, S. Smolka, and P. Lodahl, Science **327**, 1352 (2010).
31. C. R. Doerr, Front. Phys. **3**, 37 (2015).
32. A. D. Rakić, A. B. Djurišić, J. M. Elazar, and M. L. Majewski, Appl. Opt. **37**, 5271 (1998).